Acta Pharmaceutica Sinica B 2025;15(10):5036−5049

Chinese Pharmaceutical Association
Institute of Materia Medica, Chinese Academy of Medical Sciences

Acta Pharmaceutica Sinica B

www.elsevier.com/locate/apsb
www.sciencedirect.com

ORIGINAL ARTICLE

Imaging poly(ADP-ribose) polymerase-1 (PARP1) *in vivo* with ^{18}F-labeled brain penetrant positron emission tomography (PET) ligand

Xin Zhou[a,†], Jiahui Chen[a,†], Jimmy S. Patel[a,b,†], Wenqing Ran[c], Yinlong Li[a], Richard S. Van[d], Mostafa M.H. Ibrahim[e], Chunyu Zhao[a], Yabiao Gao[a], Jian Rong[a], Ahmad F. Chaudhary[a], Guocong Li[c], Junqi Hu[c], April T. Davenport[f], James B. Daunais[g], Yihan Shao[d], Chongzhao Ran[h], Thomas L. Collier[a], Achi Haider[a], David M. Schuster[a], Allan I. Levey[i], Lu Wang[c], Gabriel Corfas[e], Steven H. Liang[a,*]

[a]*Department of Radiology and Imaging Sciences, Emory University, Atlanta, GA 30322, USA*
[b]*Department of Radiation Oncology, Winship Cancer Institute of Emory University, Atlanta, GA 30322, USA*
[c]*Center of Cyclotron and PET Radiopharmaceuticals, Department of Nuclear Medicine & Key Laboratory of Basic and Translational Research on Radiopharmaceuticals, the First Affiliated Hospital of Jinan University, Guangzhou 510630, China*
[d]*Department of Chemistry and Biochemistry, University of Oklahoma, Norman, OK 73019, USA*
[e]*Kresge Hearing Research Institute, Department of Otolaryngology-Head and Neck Surgery, University of Michigan, Ann Arbor, MI 48109, USA*
[f]*Department of Physiology and Pharmacology, Wake Forest School of Medicine, Winston Salem, NC 27157, USA*
[g]*Department of Internal Medicine, Section on Infectious Diseases, Wake Forest School of Medicine, Winston Salem, NC 27157, USA*
[h]*Athinoula A. Martinos Center for Biomedical Imaging, Department of Radiology, Massachusetts General Hospital and Harvard Medical School, Boston, MI 02114, USA*
[i]*Department of Neurology, Emory University, Atlanta, GA 30322, USA*

Received 28 October 2024; received in revised form 6 May 2025; accepted 7 May 2025

This article is part of a special issue entitled: Targeted Radiopharmaceuticals published in Acta Pharmaceutica Sinica B.

*Corresponding author.
E-mail address: steven.liang@emory.edu (Steven H. Liang).
[†]These authors made equal contributions to this work.

Peer review under the responsibility of Chinese Pharmaceutical Association and Institute of Materia Medica, Chinese Academy of Medical Sciences.

https://doi.org/10.1016/j.apsb.2025.05.020
2211-3835 © 2025 The Authors. Published by Elsevier B.V. on behalf of Chinese Pharmaceutical Association and Institute of Materia Medica, Chinese Academy of Medical Sciences. This is an open access article under the CC BY-NC-ND license (http://creativecommons.org/licenses/by-nc-nd/4.0/).

KEY WORDS

Poly(ADP-ribose) polymerase-1;
PARP1;
DNA damage;
Cell death;
Positron emission tomography;
PET;
Imaging;
Fluorine 18

Abstract Poly(ADP-ribose) polymerase 1 (PARP1) is a multifunctional protein involved in diverse cellular functions, notably DNA damage repair. Pharmacological inhibition of PARP1 has therapeutic benefits for various pathologies. Despite the increased use of PARP inhibitors, challenges persist in achieving PARP1 selectivity and effective blood−brain barrier (BBB) penetration. The development of a PARP1-specific positron emission tomography (PET) radioligand is crucial for understanding disease biology and performing target occupancy studies, which may aid in the development of PARP1-specific inhibitors. In this study, we leverage the recently identified PARP1 inhibitor, AZD9574, to introduce the design and development of its ^{18}F-isotopologue ([^{18}F]AZD9574). Our comprehensive approach, encompassing pharmacological, cellular, autoradiographic, and *in vivo* PET imaging evaluations in non-human primates, demonstrates the capacity of [^{18}F]AZD9574 to specifically bind to PARP1 and to successfully penetrate the BBB. These findings position [^{18}F]AZD9574 as a viable molecular imaging tool, poised to facilitate the exploration of pathophysiological changes in PARP1 tissue abundance across various diseases.

© 2025 The Authors. Published by Elsevier B.V. on behalf of Chinese Pharmaceutical Association and Institute of Materia Medica, Chinese Academy of Medical Sciences. This is an open access article under the CC BY-NC-ND license (http://creativecommons.org/licenses/by-nc-nd/4.0/).

1. Introduction

Poly(ADP-ribose) polymerases (PARPs) constitute a family of enzymes that play an integral role in several cellular processes-most notably DNA repair[1]. Of the 18 members in the PARP family, PARP1 and PARP2 are the most abundant and contain zinc finger domains that assist in genome surveillance and DNA repair pathways[2,3]. PARP1, in particular, uniquely binds to single-stranded DNA breaks and facilitates repair by synthesizing a poly(ADP-ribose) polymer[4]. The role of PARP1 in DNA repair is intriguing, as certain tumors with mutations in homologous recombination repair mechanisms may depend on PARP1-mediated DNA repair for survival, rendering them susceptible to synthetic lethality by PARP inhibition[1]. Olaparib, the pioneering PARP1/2 inhibitor, gained US Food and Drug Administration (FDA) approval in 2014 for management of ovarian cancer with a germline breast cancer gene (BRCA) mutation[5]. Subsequently, rucaparib and niraparib received approval for ovarian cancer treatment in 2016 and 2017, respectively. Olaparib garnered further FDA approval in 2022 for treating high-risk early breast cancer and in 2023 for BRCA-mutated metastatic castration-resistant prostate cancer[6-7]. Beyond cancer, PARP inhibition has shown utility in various inflammatory disorders, including arthritis, psoriasis, colitis, asthma, diabetic complications, as well as cardiovascular and neurodegenerative diseases[8-9]. This benefit is hypothesized to stem from inhibition of PARP-mediated pro-inflammatory and apoptotic signaling pathways, and these multifaceted applications underscore the broad therapeutic potential of PARP inhibition[10-12].

Positron emission tomography (PET) is a widely-utilized functional imaging technique that allows for the non-invasive examination of *in vivo* pathophysiology through the use of positron-emitting radioactive ligands[13-15]. The most common and widely utilized radioactive isotope for PET imaging is fluorine 18 (^{18}F)[16-19]. Over the past decade, numerous PARP targeted radiotracers have emerged and have been reviewed[15,20-22]. Notable among these is [^{18}F]FluorThanatrace ([^{18}F]FTT), which has undergone first-in-human imaging studies and validated its efficacy as a biomarker for quantifying PARP expression levels, particularly in breast and ovarian cancer patients[23]. Additionally, [^{18}F]PARP-inhibitor ([^{18}F]PARPi) has been identified as a safe and feasible radiotracer for imaging head and neck cancers[24]. Furthermore, preclinical evaluation of [^{18}F]olaparib demonstrated uptake in pancreatic cell tumors, *in vitro* and within xenograft models[25]. Despite the significant progress in the development of various PARP inhibitor based radiotracers, a prevalent limitation persists in their restricted ability to penetrate the BBB[26]. This constraint impedes the assessment of PARP-specific expression and distribution in the brain, particularly in conditions such as glioma, brain metastasis, and other central nervous system (CNS) diseases involving with DNA damage/cell death. Furthermore, many of these ligands are derivatives of non-selective PARP inhibitors, such as rucaparib and olaparib, which bind to various isoforms of PARP including PARP1 and PARP2[27]. Despite being in the same family, PARP1 and PARP2 are encoded from different chromosomes and may have different physiological functions[28]. As such, inhibition of PARP2 leads to off-target side effects, such as anemia, which was a commonly seen side effect in three phase III clinical trials assessing treatment response of olaparib, rucaparib, and niraparib[29-33]. With therapeutic efficacy intimately linked to PARP1 inhibition, there is an emphasis on the development of PARP1 selective PET ligands to accurately understand target engagement.

While achieving PARP1 selectivity is crucial, another key characteristic to assess for radioligands is their ability to penetrate through the blood−brain barrier (BBB), especially to address target engagement within intracranial diseases such as primary brain cancer and metastatic brain lesions[34]. Recent advancements in BBB-penetrant PARP-targeted PET imaging include the development of [^{11}C]PyBic, which demonstrated encouraging brain permeability in rodents and nonhuman primates (NHPs)[35]. However, its selectivity for PARP1 over PARP2 requires further investigation due to its origin from veliparib, a nonselective PARP inhibitor with equipotency against both PARP1 and PARP2. Recently, Schou and colleagues[36-37] disclosed [^{11}C]AZ14193391, a radiotracer that exhibits promising ability to penetrate the BBB, albeit with an unconventional brain pharmacokinetic profile characterized by an upward time−activity curve in later time points. Similarly, [^{11}C]AZD9574 was also shown to possess the ability to penetrate the BBB while its cold compound, AZD9574, showed synergy when used with temozolomide both *in vitro* and *in vivo*[38-39]. The use of ^{11}C-labeled radiotracers typically necessitates an onsite cyclotron due to its shorter half-life ($t_{1/2}$ = 20.4 min), which may oftentimes constrain broad clinical application and commercialization. These challenges

accentuate the continuous efforts and urgent need to enhance both PARP1 selectivity and practicality of PET tracers for improved imaging precision and wider clinical utility.

Inspired by the recent disclosure of AZD9574, a fluorine-containing PARP inhibitor distinguished by its exceptional potency, selectivity to PARP1, and favorable ADME (absorption, distribution, metabolism, and excretion) properties, we postulated that an ^{18}F-isotopologue of AZD9574 may hold promise as a PARP1-selective PET radioligand with the ability to penetrate the BBB[39]. Through the strategic repurposing of AZD9547, which is presently undergoing phase I clinical trials as a therapeutic agent, into a diagnostic molecular imaging PET probe, we anticipate streamlined translation of PET imaging to clinical application. In this work, we describe the radiolabeling strategy, precursor synthesis, pharmacological and ADME characterization of [^{18}F]AZD9574. Furthermore, we provide in-depth *in vitro* validation through cellular uptake and autoradiography studies, as well as a proof-of-concept PET evaluation in NHPs, supporting the potential clinical utility of our approach.

2. Results and discussion

2.1. Chemistry

The process of ^{18}F-isotopologue labeling involves the incorporation of ^{18}F radionuclide into the molecule of interest without altering the remainder of the original structure. As shown in Scheme 1, compound **5** (AZD9574) was synthesized following a previously published synthetic scheme[39]. Compound **8**, the radiolabeling precursor, was also prepared in a similar fashion. In all, compounds **5** and **8**, were synthesized from their corresponding methyl picolinates in four steps with an overall yield of 13% and 21%, respectively. The purity of AZD9574 and compound **8** was confirmed by HPLC (Supporting Information Figs. S1 and S2).

2.2. Pharmacology

The pharmacology, physiochemical, and ADME properties of compound **5** are summarized in Table 1. To validate the potency and selectivity of compound **5** against PARP1, we performed enzymatic assays using commercially available PARP1 and PARP2 testing kits (see Supporting Information). Compound **5** exhibited high potency against PARP1 with an IC_{50} value of 1.20 nmol/L, while demonstrating an IC_{50} value toward PARP2 exceeding 1.0 μmol/L. This showcased a >800-fold selectivity toward PARP1 over PARP2. Compound **5** exhibited favorable physiochemical attributes for BBB penetration, including molecular weight of 428.4, cLog*P* value of 1.83 and topological polar surface area (TPSA) of 89.4. The blood−brain barrier permeability (logBB) value was predicted as −0.30 using ACD/Percepta™, and the CNS multiparameter optimization (MPO) score was determined as 4.90, both falling within the preferred range for BBB permeability[40-42]. Furthermore, an *in vitro* Pg-P efflux assay of compound **5** demonstrated high passive permeability (P_{app} AB: 42.5×10^{-6} cm/s) and a low efflux ratio (MDR1 BA/AB: 0.85). Lipophilicity measurement was completed by the 'shake-flask' method with a $logD_{7.4}$ value of 1.87. A protein binding study indicated that compound **5** possessed reasonable unbound fractions in the plasma of rats (6.9%, free) and humans (2.6%, free). Additionally, compound **5** exhibited *in vitro* human ether-a-go-go-related gene (hERG) channel safety with $IC_{50} > 100$ μmol/L and CellTiter-Glo luminescent cell viability assay in HepG2 cells with $IC_{50} > 100$ μmol/L. No significant interactions with metabolic cytochrome P450 (CYP) isoforms were identified (all six major CYP450s $IC_{50} > 5$ μmol/L). These favorable pharmacological and ADME properties affirmed compound **5** as the lead molecule for further evaluation. For IC_{50} curves of AZD9574 against PARP1 and PARP2, see Supporting Information Fig. S3.

2.3. Molecular docking study

To elucidate the ligand−protein interaction between the lead compound **5** and PARP1, we established a homology model and performed molecular docking studies based on previously published PARP1 X-ray co-crystal structures. The structural data of PARP1 utilized in this study were retrieved from the Protein Data Bank (PDB 7ONT)[43]. A favorable binding position in the catalytic domain of PARP1 (residues 788−1014) was characterized by a quinoxalin-2(1*H*)-one moiety interacting with residues G863,

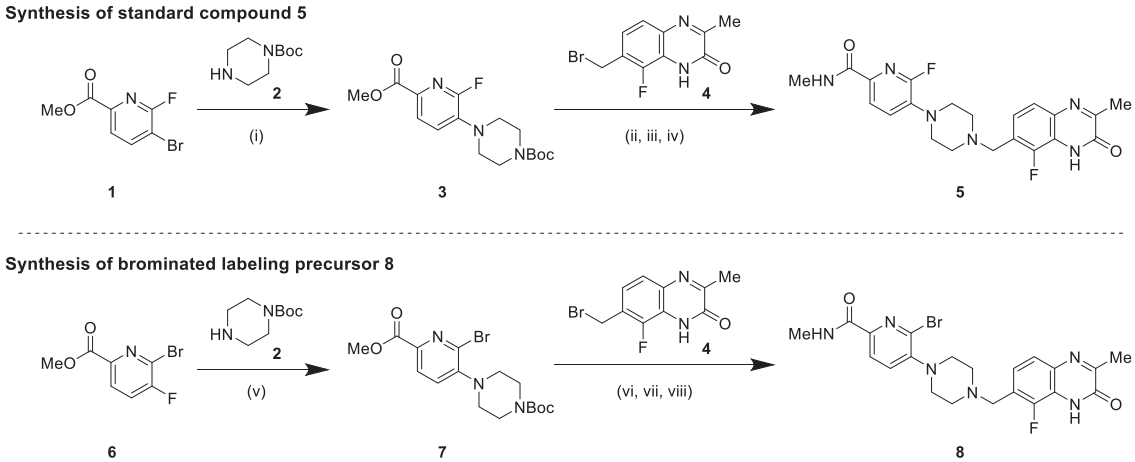

Scheme 1 Synthesis of compound **5** (AZD9574) and its bromide labeling precursor compound **8**. Conditions: (i) *N-Boc* piperazine, Pd-RuPhos-G3, Cs_2CO_3, 1,4-dioxane, 100 °C, 24 h, 27%; (ii) HCl in 1,4-dioxane (4.0 mol/L), 6 h, rt, used without purification; (iii) DIPEA, MeCN, 80 °C, 12 h; (iv) $MeNH_2$ in THF (2.0 mol/L), EtOH, 80 °C, 12 h, 49%; (v) K_2CO_3, DMF, 130 °C, 12 h, 57%; (vi) HCl in 1,4-dioxane (4.0 mol/L), 6 h, rt, used without purification; (vii) DIPEA, MeCN, 80 °C, 12 h; (viii) $MeNH_2$ in THF (2.0 mol/L), EtOH, 80 °C, 12 h, 37%.

Table 1 Pharmacology, physiochemical and ADME properties of compound **5**.

Iterm	PARP1 IC_{50} (nmol/L)	PARP2 IC_{50} (nmol/L)	PARP1/2 selectivity
AZD9574	1.2	>1000	>800
Control (veliparib)	2.6	7.0	2.7
Molecular weight	cLog*P*	Log*D*	Topological polar surface area (TPSA)
428.44	1.83	1.87	89.4
BBB permeability LogBB	Multiparameter optimization (MPO) score	Passive permeability P_{app} AB ($\times 10^{-6}$ cm/s)	Efflux ratio
−0.3	4.9	42.5	0.85
Protein binding		Mean (% free)	
Human plasma		2.6	
Rat plasma		6.9	
Cytochrome P450 (CYP) isoforms		IC_{50}	
CYP1A2, CYP2D6, CYP2C19, CYP3A4, CYP2C9, CYP19A		All>5 μmol/L	
hERG IC_{50} (μmol/L)		HepG2 IC_{50} (μmol/L)	
>100		>100	

S904, and Y907, and a picolinamide moiety interacting with I879 (Fig. 1A). Specifically, the quinoxalin-2(1*H*)-one moiety formed two hydrogen bonds with the peptide backbone of residue G863 (2.871 and 2.006 Å, respectively), and one hydrogen bond with the sidechain of residue S904 (2.912 Å). Additionally, $\pi-\pi$ stacking was observed between this moiety and residue Y908 with a distance of 3.336 Å. In the loop region, a picolinamide moiety formed a hydrogen bond with the peptide backbone of residue I879 (2.133 Å). The binding pose suggests that the quinoxaline-2(1*H*)-one moiety may preferentially orient towards the hydrophobic region with the fluorinated substituent pointing toward a polar region. Additionally, the picolinamide scaffold interacts with the charged region within the binding pocket with its fluorinated substituent located in a positively charged region (Fig. 1B). This molecular docking study provides valuable insights into the specific interactions that contribute to the binding affinity between compound **5** and PARP1, and additionally presents opportunities to guide medicinal chemistry optimization of ligand interactions.

2.4. *Radiochemistry*

Encouraged by the promising potency, selectivity, and ADME attributes, we next performed the synthesis of ^{18}F-labeled isotopologue of compound **5** ([^{18}F]AZD9574) (The full screened conditions, Supporting Information Table S1). As outlined in Fig. 2A, [^{18}F]AZD9574 was synthesized *via* a direct nucleophilic aromatic substitution (S_NAr) displacement reaction of **8**. The radiofluorination was performed by heating the mixture of **8** and azeotropically dried [^{18}F]fluoride with various bases and solvents. Initially, production of [^{18}F]AZD9574 was attempted using K_2CO_3/K_{222} (Kryptofix 222) system in the presence of dimethylformamide (DMF) at 150 °C for 20 min (Fig. 2, Entry 1), but this did not yield the desired product. Similar results were obtained when switching the solvent to DMSO (Fig. 2, Entry 2). Subsequent attempts with tetraethylammonium bicarbonate (TEAB) in DMSO as the solvent showed an increased radiochemical yield (RCY) to 18% (Fig. 2, Entry 3). However, even in the presence of the increased amount of precursor **8** (2.0 mg), a lower RCY of 11% was detected with DMF as the solvent (Fig. 2, Entry 4), suggesting DMSO to be the solvent of choice. Consequently, a higher temperature was applied when DMSO was used as the solvent, resulting in 25% RCY (Fig. 2, Entry 5). In addition, reducing the precursor **8** to 0.5 mg resulted in a slightly lower RCY (Fig. 2, Entry 6). Under optimal conditions (Fig. 2, Entry 5), [^{18}F]AZD9574 was obtained with 15% RCY (isolated and non-decayed corrected, confirmed by co-injection with AZD9574, Supporting Information Fig. S4) with excellent radiochemical purity (>99%)

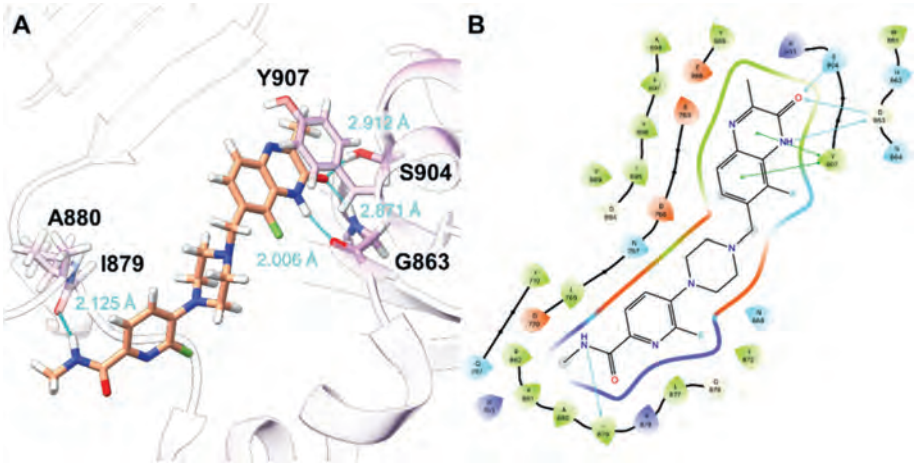

Figure 1 Molecular docking structure of compound **5** onto PARP1 (PDB ID: 7ONT). (A) 3D ligand interaction and (B) 2D interaction plot. The hydrogen bonding interactions between compound **5** and PARP1 residues are indicated by turquoise blue lines in Panel A and Panel B.

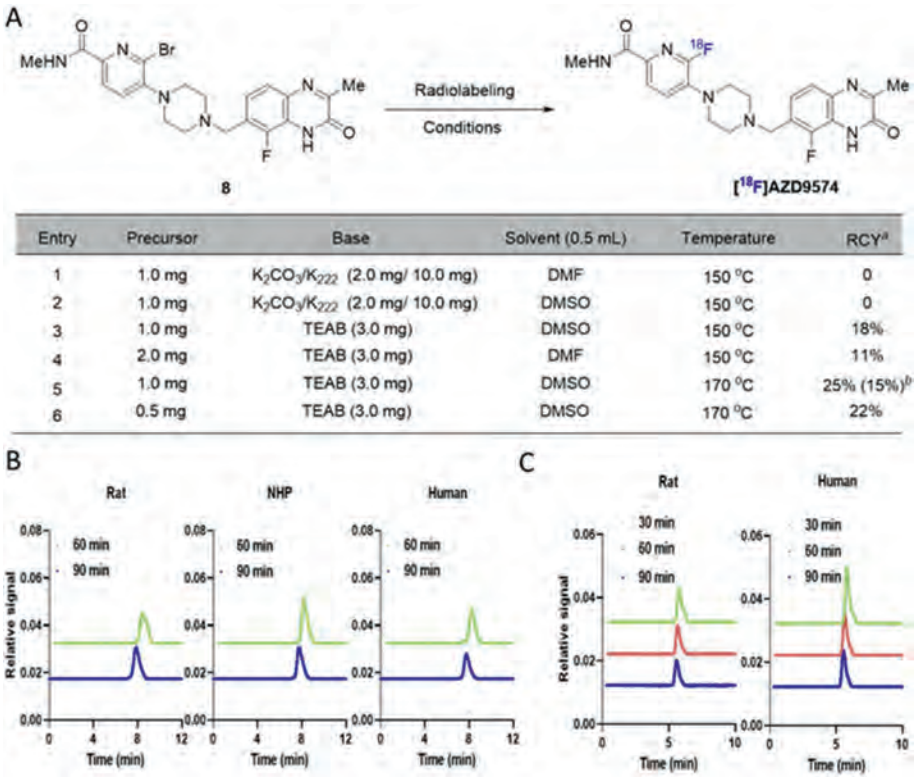

Entry	Precursor	Base	Solvent (0.5 mL)	Temperature	RCY[a]
1	1.0 mg	K_2CO_3/K_{222} (2.0 mg/ 10.0 mg)	DMF	150 °C	0
2	1.0 mg	K_2CO_3/K_{222} (2.0 mg/ 10.0 mg)	DMSO	150 °C	0
3	1.0 mg	TEAB (3.0 mg)	DMSO	150 °C	18%
4	2.0 mg	TEAB (3.0 mg)	DMF	150 °C	11%
5	1.0 mg	TEAB (3.0 mg)	DMSO	170 °C	25% (15%)[b]
6	0.5 mg	TEAB (3.0 mg)	DMSO	170 °C	22%

Figure 2 Radiosynthesis and optimization of [^{18}F]AZD9574 as well as stability testing. [a]Radiochemical yield (determined by radio-HPLC, non-decay-corrected). [b]The value in parenthesis refers to an average isolated radiochemical yield (non-decay-corrected, $n = 4$); (A) Radiosynthesis and optimization of [^{18}F]AZD9574; (B) Stability of radioligand [^{18}F]AZD9574 in plasma; and (C) in liver microsomes of several species (rat, NHP, and human).

and greater than 37 GBq/μmol molar activity. Moreover, [^{18}F]AZD9574 exhibited exceptional stability (>95%) and no radiolysis in various formulations and media, including plasma and liver microsome across several species within 90 min, *in vitro* (rat, NHP, and human; Fig. 2B and C; For stability in PBS, Supporting Information Fig. S5).

2.5. *Cellular uptake studies*

To assess specific binding at the cellular level, *in vitro* cell uptake assays of [^{18}F]AZD9574 were conducted in PC3 cell lines, as shown in Fig. 3. Validation of PARP1 expression was first confirmed through Western blot analysis using a commercially available PARP1 antibody (Supporting Information Fig. S6). The uptake of [^{18}F]AZD9574 in PC3 cells demonstrated a rapid increase within the initial 5 min of incubation, reaching its peak at 30 min (Fig. 3A). [^{18}F]AZD9574 uptake displayed a dose-dependent reduction (from 12.4% to 83.3% blockade) with escalating doses of compound AZD9574 (Fig. 3B). Furthermore, olaparib significantly attenuated the uptake signal of [^{18}F]AZD9574 (Fig. 3C). In contrast, the PARP2 specific blocking reagent UPF-1035 exhibited no inhibitory effect on [^{18}F]AZD9574 uptake (Fig. 3D). These findings collectively affirm the robust specific binding of [^{18}F]AZD9574 to PARP1 and excellent selectivity for PARP1 over PARP2 at the cellular level.

2.6. *In vitro autoradiography*

To further investigate the specific binding of [^{18}F]AZD9574 to PARP1, *in vitro* autoradiography was conducted on rodent and NHP brain sections (Figs. 4–6). As illustrated in Fig. 4A and B, baseline studies with [^{18}F]AZD9574 revealed heterogeneity in radioactivity levels across various rat brain regions. The highest uptake was observed in the cerebellum and hippocampus, while the lowest uptake was observed in the pons. The radioactive distribution profile of [^{18}F]AZD9574 corresponded with the PARP1 expression pattern in rodents. Blocking by PARP inhibitors (AZD2461, olaparib, pamiparib, rucaparib, veliparib, AZD9574 at 10 μmol/L), showed that the accumulation of radioactivity in all brain regions was significantly reduced by greater than 85% (Fig. 4C). Notably, brain regions with relatively high levels of PARP1 exhibited a much higher reduction in radioactive uptake, such as the cerebellum, hippocampus and cerebral cortex. To distinguish the binding specificity of [^{18}F]AZD9574 targeting PARP1 and PARP2, a blocking study was conducted with a PARP2 selective inhibitor, UPF-1035, under 10 μmol/L high concentration. In contrast to the significant blockade observed in the presence of other PARP1 inhibitors, UPF-1035 blocking exhibited only a modest signal reduction and displayed a heterogeneous distribution analogous to baseline conditions (Fig. 4D).

With promising *in vitro* autoradiography results obtained with rat brain sections, we extended our investigation to NHP brain sections (Fig. 5A). *In vitro* autoradiography was conducted on NHP cerebellum brain sections under baseline and blocking conditions with PARP inhibitors (AZD9574, Olaparib), and PARP2 inhibitor UPF-1035 at the concentration of 10 μmol/L. Similar to the outcomes observed in rat brain sections, [^{18}F]AZD9574 exhibited high uptake in the cerebellum, with a substantial uptake reduction when pre-treated with AZD9574 and Olaparib (Fig. 5B). Under blocking conditions with UPF-1035

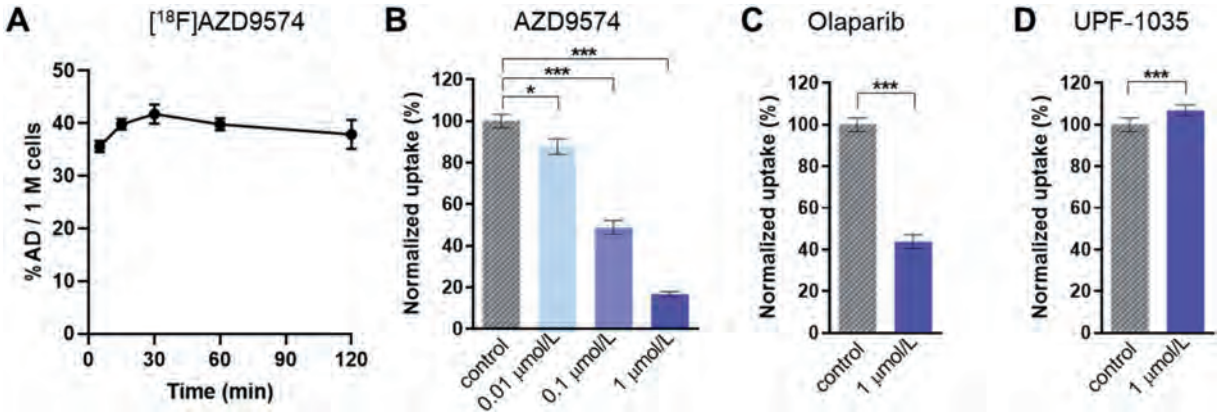

Figure 3 Cell uptake assay of [^{18}F]AZD9574 in PC3 cell lines. (A) Cell uptake at different time points (5, 15, 30, 60 and 120 min, respectively); (B) Baseline and blocking studies in the presence of AZD9574 (0.01, 0.1 and 1 μmol/L, respectively); (C) Baseline and blocking studies in the presence of olaparib (1 μmol/L); and (D) Baseline and blocking studies in the presence of UPF-1035 (1 μmol/L), a PARP2 inhibitor. %AD = % added dose in the cell uptake assays. All data are mean ± SD, $n = 3$. Statistical significance is indicated as asterisks: $^{*}P \leq 0.05$, $^{***}P \leq 0.001$.

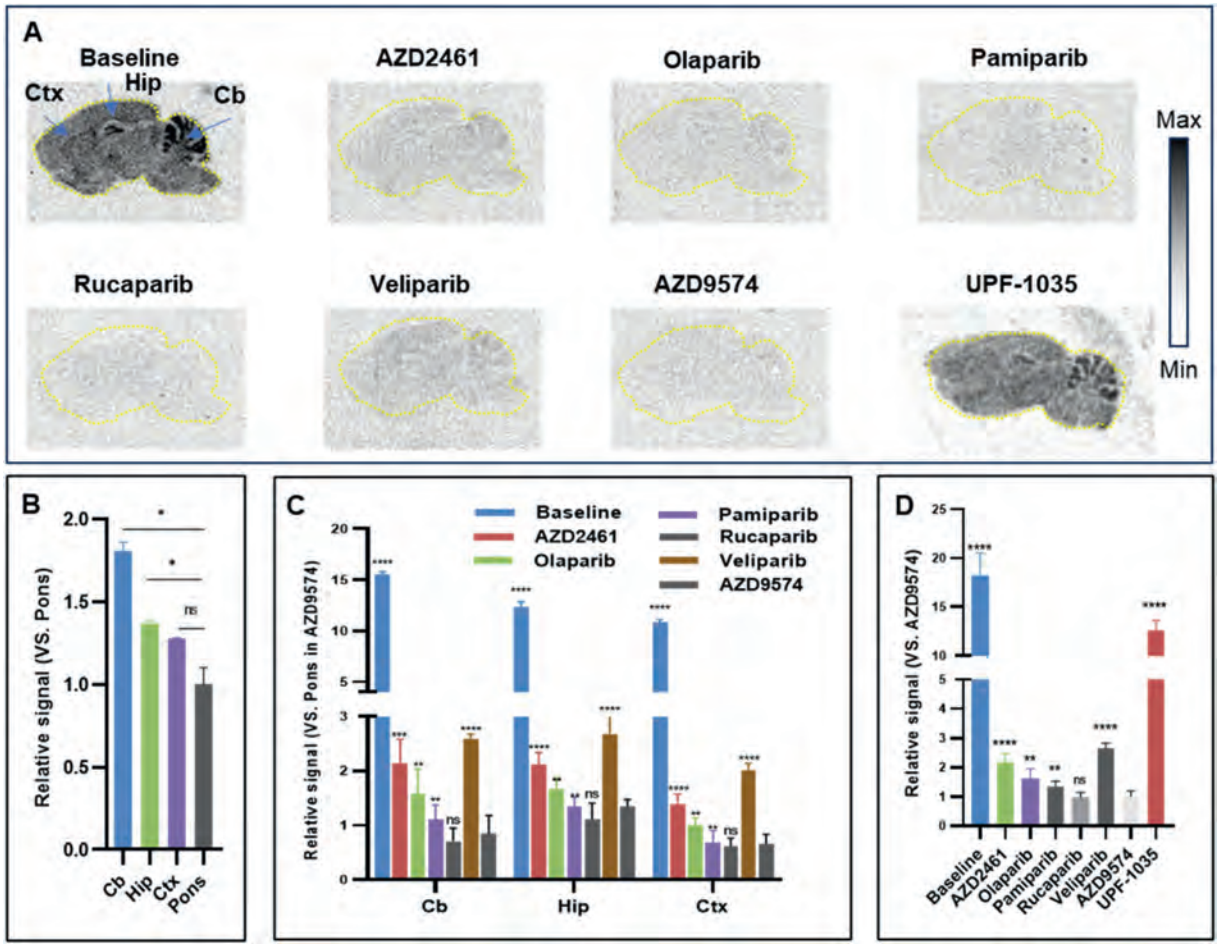

Figure 4 Autoradiography studies of radioligand [^{18}F]AZD9574 on rat brain sections. (A) Baseline and blocking autoradiograms in the presence of PARP1 inhibitors (AZD2461, olaparib, pamiparib, rucaparib, veliparib, AZD9574) and PARP2 inhibitor (UPF-1035) at 10 μmol/L concentration; (B) Quantification of radioactivity in different brain regions under baseline conditions, consistent with PARP1 expression profile; (C) Quantification of radioactivity uptake in regional brain sections (cerebellum, hippocampus and cortex) under baseline and blocking conditions using PARP1 inhibitors (10 μmol/L) in panel A; and (D) Quantification of radioactivity uptake in whole brain sections under baseline and blocking conditions using PARP1 and PARP2 inhibitors (10 μmol/L) in panel A. All data are mean ± SD, $n = 3$. Statistical significance is indicated as asterisks: $^{*}P \leq 0.05$, $^{***}P \leq 0.001$, $^{****}P \leq 0.0005$, and ns = no significant. Ctx = cerebral cortex; Hip = hippocampus; Cb = cerebellum.

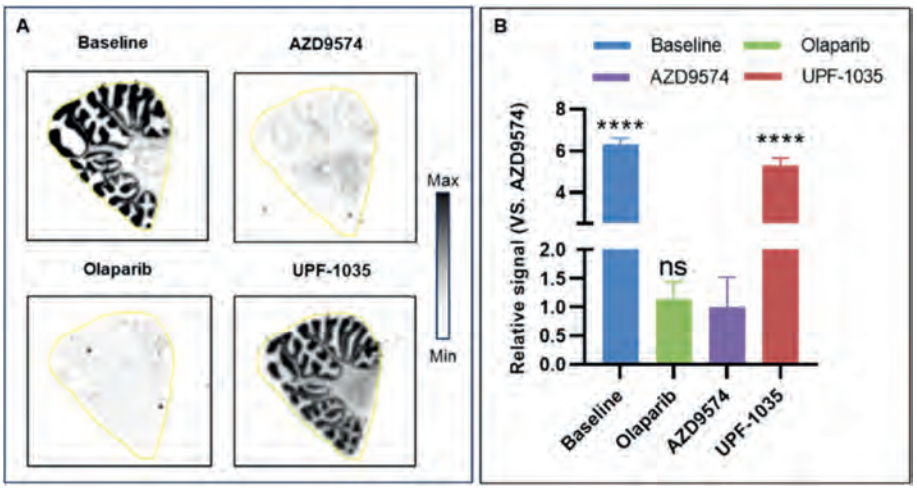

Figure 5 Autoradiography of radioligand [^{18}F]AZD9574 on NHP cerebellum brain sections. (A) Baseline and blocking autoradiograms in the presence of PARP inhibitor (AZD9574, olaparib) and PARP2 inhibitor (UPF-1035) at 10 μmol/L concentration; and (B) Quantification of radioactivity uptake in the cerebellum under baseline and blocking conditions. All data are mean ± SD, $n = 3$. Statistical significance is indicated as asterisks: $^{**}P \leq 0.01$, $^{****}P \leq 0.0005$.

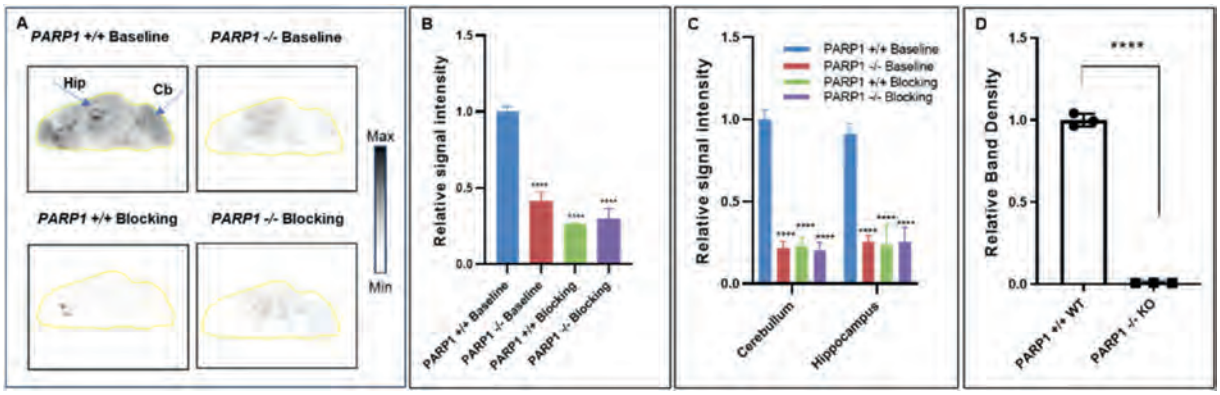

Figure 6 Autoradiography of radioligand [^{18}F]AZD9574 on PARP1 knockout mouse brain sections. (A) Baseline and blocking autoradiograms in wild-type *PARP1*$^{+/+}$ and *PARP1*$^{-/-}$ knockout mouse brain tissues with or without with olaparib (10 μmol/L); (B) Quantification of radioactivity in the mouse whole brain under baseline and blocking conditions; (C) Quantification of radioactivity in the mouse cerebellum and hippocampus under baseline and blocking conditions; and (D) Quantification of PARP1 expression in wild-type *PARP1*$^{+/+}$ and *PARP1*$^{-/-}$ knockout mouse brain tissues by Western blot analysis. All data are mean ± SD, $n = 3$. Statistical significance is indicated as asterisks: $^{*}P \leq 0.05$, $^{****}P \leq 0.0005$, and ns = no significant.

(10 μmol/L), radioactivity accumulation in the cerebellum showed an approximate 20% reduction. These results with NHP sections further support the excellent *in vitro* specific binding of [^{18}F] AZD9574.

To further highlight the specific binding of [^{18}F]AZD9574, *in vitro* autoradiography was conducted using *PARP1*$^{-/-}$ knockout mice and their corresponding wild-type counterpart *PARP1*$^{+/+44}$. As depicted in Fig. 6A, [^{18}F]AZD9574 exhibited characteristic high uptake in the cerebellum and hippocampus in wild-type mice, similar to the baseline conditions observed in rat brain sections. The radioactivity accumulation was significantly reduced by greater than 65% in the whole brain region of *PARP1*$^{-/-}$ knockout (Fig. 6B), which is consistent with our biological validation of PARP1 expression in the mouse brain using Western blot analysis (Fig. 6D). Brain regions featuring relatively high levels of PARP1 expression, exhibited a much higher reduction of radioactive uptake, such as the cerebellum and hippocampus as shown in Fig. 6C. In all, autoradiograph studies conducted on rat and NHP brain tissues, coupled with validation using PARP1 knockout mouse models, clearly confirm high specific binding and excellent selectivity towards PARP1 by [^{18}F]AZD9574.

2.7. *NHP PET imaging*

The compelling *in vitro* performance and favorable ADME properties motivated us to perform a proof-of-concept evaluation of [^{18}F]AZD9574 in an NHP PET study. PET image acquisition was initiated by the administration of [^{18}F]AZD9574 (4.05 ± 0.54 mCi) for both baseline and blocking scans. Initially, two baseline scans were conducted on two different animals, followed by two blocking scans on the same animal under two different doses of AZD9574 (0.05 and 0.5 mg/kg, respectively).

As illustrated in Fig. 7A, baseline studies of [^{18}F]AZD9574 showed moderate-to-good brain penetration with heterogeneous

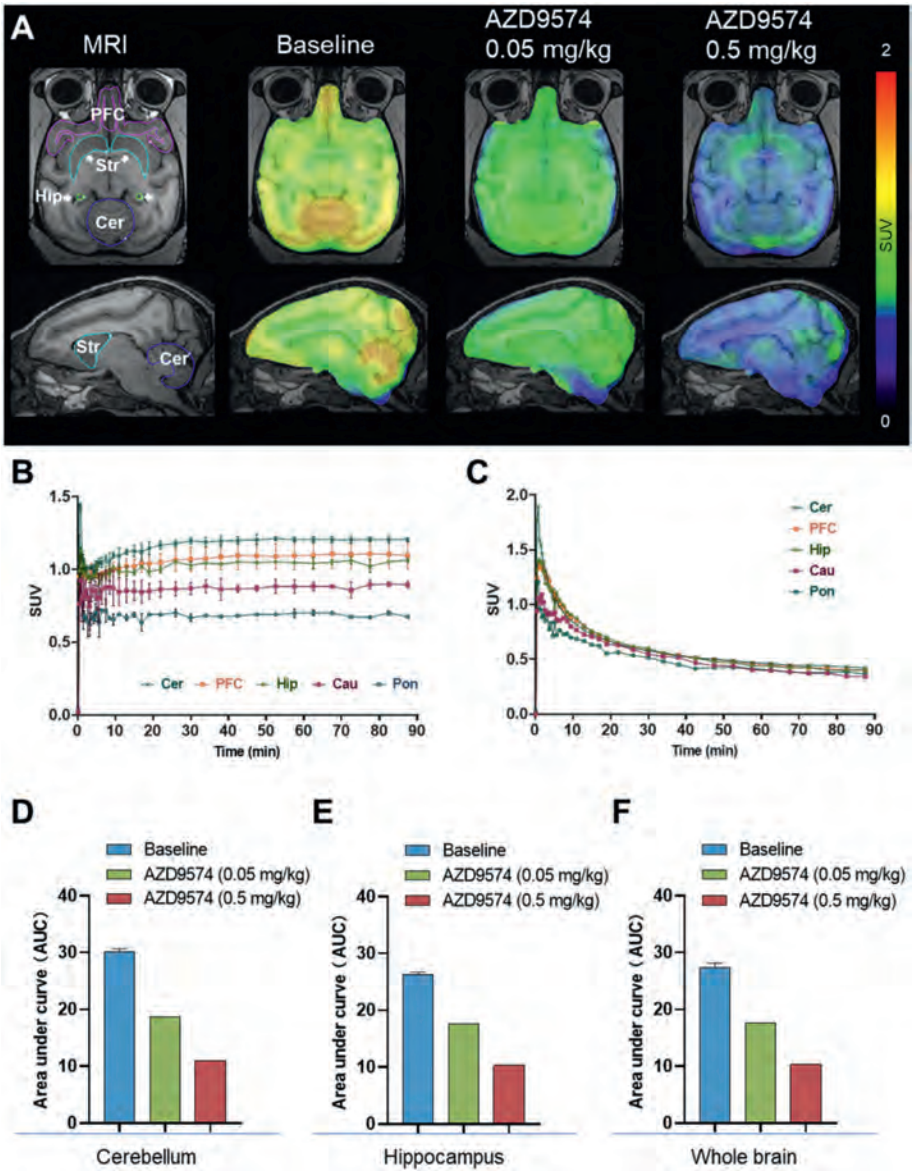

Figure 7 PET studies of [^{18}F]AZD9574 in rhesus monkey brains. (A) Representative magnetic resonance (MR) and PET images (summed 60−90 min) of [^{18}F]AZD9574 under baseline and blocking conditions; (B) Time−activity curves (TACs) of [^{18}F]AZD9574 in various brain regions of interest under baseline conditions (n = 2); (C) Time−activity curves (TACs) of [^{18}F]AZD9574 under blocking conditions (AZD9574, 0.5 mg/kg, n = 1); (D−F) Quantification of baseline and blocking conditions using area under curve (60−90 min) in the cerebellum, hippocampus and whole brain (baseline, n = 2; blocking n = 1 per condition). Cer = cerebellum; PFC = prefrontal cortical; Hip = hippocampus; Cau = caudate; Pon = pons.

radioactivity levels across various NHP brain regions. Five representative regions of interest are delineated in Fig. 7B. Radioactivity levels in all brain regions steadily increased up to 30 min post injection before plateauing. The cerebellum exhibited the highest radioactivity uptake at 1.20 SUV, followed by the prefrontal cortex (1.10 SUV), hippocampus (1.05 SUV), and caudate nucleus (0.88 SUV). The lowest radioactivity level was observed in the pons (0.67 SUV), which was similar to the autoradiography results in rodents. We next conducted blocking experiments for [^{18}F]AZD9574 under low and high inhibitor doses in the same animal. As depicted in Fig. 7C, pretreatment with AZD9574 (0.05 and 0.50 mg/kg, respectively) remarkably diminished radioactivity in various brain regions in a dose-dependent manner. Three representative regions of interest, namely the whole brain, cerebellum, and hippocampus were quantified by measuring the area under curve between 60 and 90 min post injection (Fig. 7D−F). For example, in the cerebellum, radioactivity accumulation was reduced by 37.7% when blocked by a low dose (0.05 mg/kg) of AZD9574 and 63.4% when blocked by a high dose of 0.5 mg/kg (Fig. 7D). Similar trends were observed in the hippocampus (Fig. 7E) and whole brain (Fig. 7F). These results collectively indicate reasonable brain permeability and excellent binding specificity of [^{18}F]AZD9574 within NHPs *in vivo*.

To further quantify the specific binding of [^{18}F]AZD9574, we conducted an analysis of non-displaceable binding potential (BP_{ND}) values using a simplified reference tissue model (SRTM)[45-46]. The pons was chosen as a pseudo reference region due to its minimal radiotracer uptake as evidenced in time−activity curve profiles. As illustrated in Fig. 8A, the BP_{ND}

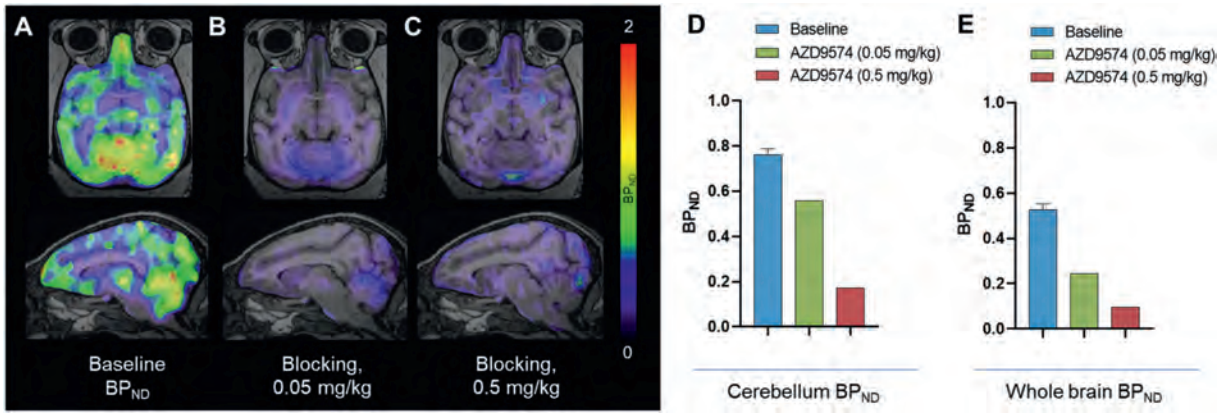

Figure 8 Parametric images and binding potentials of [^{18}F]AZD9574 in the NHP brain. (A) Baseline studies of [^{18}F]AZD9574 (n = 2); (B) Blocking conditions: AZD9574 (0.05 mg/kg, iv, n = 1); (C) Blocking conditions: AZD9574 (0.5 mg/kg, iv, n = 1); (D) Quantification of BP_{ND} for baseline and blocking conditions in the cerebellum; and (E) Quantification of BP_{ND} for baseline and blocking conditions in the whole brain.

image and bound signal of [^{18}F]AZD9574 in NHP brains decreased in order from cerebellum, hippocampus, caudate and pons under baseline conditions. This distribution pattern aligns with the known expression of PARP1 in the brain, corroborated by *in vitro* autoradiography results presented in Figs. 5−7[47]. The observed BP_{ND} values exhibited a substantial decrease under blocking conditions in a dose response manner following pretreatment with AZD9574 at doses of 0.05 mg/kg and 0.5 mg/kg (Fig. 8B and C). Notably, radioactivity uptake diminished by 26.6%−77.5% under both blocking doses in the cerebellum and 53.5%−81.6% in the whole brain (Fig. 8D and E). In addition, the parametric brain image demonstrated a significant reduction in signal heterogeneity under these blocking conditions. Collectively, these results further affirm the ability of [^{18}F]AZD9574 to penetrate through the BBB *in vivo*.

3. Conclusions

We present the synthesis and preclinical assessment of [^{18}F]AZD9574, a novel PET radioligand derived from a second generation PARP1-selective inhibitor, AZD9574. The synthesis of [^{18}F]AZD9574 was efficiently achieved through a straightforward and reproducible S_NAr reaction with 25% RCY and greater than 1.0 Ci/μmol molar activity. [^{18}F]AZD9574 demonstrated favorable pharmacological and ADME characteristics, displaying PARP1 selectivity in both *in vitro* and *in vivo* experiments. Furthermore, while its potential was underscored by evidence of BBB penetrance similar to prior studies, its favorable fluorine-18 decay profile affords broader clinical utility. These findings collectively suggest that [^{18}F]AZD9574 may be a promising candidate for future translational studies and an excellent lead compound in medicinal chemistry for balancing potency, selectivity and brain kinetics. Further evaluation in disease models, including CNS and oncological applications, has the potential to unveil valuable insights into the mechanistic role of PARP1 during disease progression and/or in response to therapeutic interventions.

4. Experimental

4.1. General information

The experimental procedures were conducted as previous reports[42,45] with minor modifications. All chemicals were purchased from commercial suppliers and used in the synthesis without further purification. The NMR spectra were collected on a 600 or 400 MHz Inova spectrometer (Varian Medical Systems, Palo Alto, USA) at room temperature. Specifically, ^{1}H NMR spectra was obtained at 600 or 400 MHz, and ^{19}F NMR spectra was obtained at 376 MHz. ^{1}H NMR chemical shifts were determined relative to internal $(CH_3)_4Si$(TMS) at δ 0.00 ppm. ^{19}F NMR chemical shifts were determined relative to $CFCl_3$ at δ 0.00 ppm. Chemical shifts (δ) were reported in ppm, and coupling constants were reported in Hz. The multiplicities are abbreviated as follows: s (singlet), d (doublet), t (triplet), m (multiplet), br (broad signal), dd (doublet of doublets), and so forth. High-resolution mass data were recorded on a high-resolution mass spectrometer in the ESI mode. High purities (≥95%) were also determined for all final compounds by reverse-phase HPLC. All animal studies were carried out in accordance with our institutional IACUC protocols and ethical guidelines. IAMEND202400000623, Institutional Animal Care and Use Committee of Emory University.

4.1.1. Chemistry

*4.1.1.1. Synthesis of tert-butyl 4-(2-fluoro-6-(methoxycarbonyl) pyridin-3-yl)piperazine-1-carboxylate (**3**).* A round bottom flask was charged with methyl 5-bromo-6-fluoropicolinate (**1**, 234.0 mg, 1.0 mmol), *tert*-butyl 1-piperazinecarboxylate (372.6 mg, 2.0 mmol), RuPhos-Pd-G3 (81.7 mg, 0.10 mmol, 10%), Cs_2CO_3 (651.6 mg, 2.0 mmol), and dissolved with 1,4-dioxane (5.0 mL). The reaction mixture was maintained at 100 °C for 24 h. Upon completion, the reaction mixture was poured into 100 mL water. The aqueous phase was then extracted with EtOAc (50 mL × 3). The organic phase was combined and washed with saturated brine and dried with anhydrous Na_2SO_4. The organic phase was removed under reduced pressure, the residue was subjected to flash chromatography (Hexanes:EtOAc = 10:1) to yield title compound 92.0 mg, slight yellow solid, 27% yield. ^{1}H NMR (600 MHz, $CDCl_3$) δ 8.06 (dd, J = 8.8, 1.7 Hz, 1H), 7.26 (d, J = 9.5 Hz, 1H), 3.99 (d, J = 1.7 Hz, 3H), 3.61 (t, J = 5.2 Hz, 4H), 3.40 (t, J = 5.1 Hz, 4H), 1.47 (s, 9H). ^{19}F NMR ($CDCl_3$, 376 MHz): δ (ppm)−69.2 (s, 1F).

*4.1.1.2. Synthesis of 6-fluoro-5-(4-((5-fluoro-2-methyl-3-oxo-3,4-dihydroquinoxalin-6-yl)methyl)piperazin-1-yl)-N-methylpicolinamide (**5**).* To a round bottom flask, *tert*-butyl 4-(2-fluoro-6-(methoxycarbonyl)pyridin-3-yl)piperazine-1-carboxylate

(84.8 mg, 0.25 mmol) was charged and dissolved with 5.0 mL MeOH. Then HCl solution (4.0 mol/L in 1,4-dioxane, 2.0 mL) was injected to reaction mixture and allowed to stir under room temperature for 6 h. The organic solvent was removed under reduced pressure and the residue was redissolved in MeCN (2.0 mL), then 7-(bromomethyl)-8-fluoro-3-methylquinoxalin-2(1*H*)-one (67.8 mg, 0.25 mmol) and *N*,*N*-diisopropylethylamine (DIPEA) (129.2 mg, 1.0 mmol, 1.7 mL) were added, and the reaction mixture was maintained at 80 °C for additional 12 h. When starting material was completely consumed, the organic solvent was removed under reduced pressure. The residue was redissolved in 5.0 mL ethanol and $MeNH_2$ (2.0 mol/L in THF, 2.0 mL) was added, then the reaction mixture was then stirred under 80 °C for an additional 12 h. After removing the organic solvent, the crude product was purified by flash chromatography (EtOAc:MeOH = 10:1), the title compound was obtained 52.5 mg, slight brown solid, 49% yield. ^{1}H NMR ($CDCl_3$, 400 MHz): δ (ppm) 9.25−9.38 (m, 1H), 7.95−8.02 (m, 1H), 7.55−7.64 (m, 1H), 7.45−7.53 (m, 1H), 7.28−7.38 (m, 2H), 3.71−3.83 (m, 2H), 3.24 (br, 4H), 3.00 (d, J = 5.2 Hz, 3H), 2.70 (br, 4H), 2.59−2.64 (m, 3H); ^{19}F NMR ($CDCl_3$, 376 MHz): δ (ppm)−72.4 (s, 1F), −141.1 (s, 1F). HRMS (ESI): exact mass Calcd. for $C_{21}H_{23}F_2N_6O_2$ $[M+H]^+$, 429.18451; found, 429.18501.

*4.1.1.3. Synthesis of tert-butyl 4-(2-bromo-6-(methoxycarbonyl) pyridin-3-yl)piperazine-1-carboxylate (**7**).* A round bottom flask was charged with methyl 6-bromo-5-fluoropicolinate (**6**, 234.0 mg, 1.0 mmol), *tert*-butyl 1-piperazinecarboxylate (372.6 mg, 2.0 mmol) and dissolved with 5.0 mL DMF. The reaction mixture was maintained at 130 °C overnight, and the progress was monitored by TLC. After 12 h, the reaction mixture was poured into 200 mL of water. The aqueous phase then extracted with EtOAc (50 mL × 3). The organic phase was then combined and washed with saturated brine and dried with anhydrous Na_2SO_4. The organic phase was removed under reduced pressure, the residue was subjected to flash chromatography (Hexanes:EtOAc = 10:1) to yield title compound 229.0 mg, slight yellow solid, 57% yield. ^{1}H NMR (400 MHz, $CDCl_3$) δ 8.05 (dd, J = 8.1, 0.5 Hz, 1H), 7.30 (d, J = 8.2 Hz, 1H), 3.96 (d, J = 0.5 Hz, 3H), 3.67−3.60 (m, 4H), 3.14−3.07 (m, 4H), 1.48 (s, 9H).

*4.1.1.4. Synthesis of 6-bromo-5-(4-((5-fluoro-2-methyl-3-oxo-3,4-dihydroquinoxalin-6-yl)methyl)piperazin-1-yl)-N-methylpicolinamide (**8**).* To a round bottom flask, *tert*-butyl 4-(2-bromo-6-(methoxycarbonyl)pyridin-3-yl)piperazine-1-carboxylate (100.1 mg, 0.25 mmol) was charged and dissolved with 5.0 mL MeOH. Then HCl solution (4.0 mol/L in 1,4-dioxane, 2.0 mL) was injected to the reaction mixture and allowed to stir at room temperature for 6 h. Then the organic solvent was removed under reduced pressure and the residue was redissolved in MeCN (2.0 mL), then 7-(bromomethyl)-8-fluoro-3-methylquinoxalin-2(1*H*)-one (67.8 mg, 0.25 mmol) and DIPEA (129.2 mg, 1.0 mmol, 1.7 mL) were added, and the reaction mixture was maintained at 80 °C for additional 12 h. When starting material was fully consumed, the organic solvent was removed under reduced pressure. The residue was redissolved in 5.0 mL ethanol with $MeNH_2$ (2.0 mol/L in THF, 2.0 mL), then the reaction mixture was stirred under 80 °C for an additional 12 h. After removing the organic solvent, the crude product was purified by flash chromatography (EtOAc:MeOH = 10:1), the title compound was obtained 45.5 mg, slight brown solid, 37% yield. ^{1}H NMR (600 MHz, DMSO) δ 12.48−12.30 (br, s, 1H, NH), 8.38 (t, J = 4.9 Hz, 1H, NH), 7.91 (d, J = 8.2 Hz, 1H), 7.59 (d, J = 8.2 Hz, 1H), 7.49 (d, J = 8.3 Hz, 1H), 7.26 (t, J = 7.6 Hz, 1H), 3.68 (d, J = 6.4 Hz, 2H), 3.05 (s, 4H), 2.75 (dd, J = 4.9, 1.8 Hz, 4H), 2.62−2.51 (m, 3H), 2.37 (d, J = 6.8 Hz, 3H). ^{19}F NMR ($CDCl_3$, 376 MHz): δ (ppm) −135.5 (s, 1F). HRMS (ESI): exact mass Calcd. for $C_{21}H_{23}{}^{79}BrFN_6O_2$ $[M+H]^+$, 489.10444; found, 489.10478.

4.1.1.5. Radiosynthesis of [^{18}F]AZD9574. The produced [^{18}F]F^- was mixed with a solution of TEAB (tetraethylammonium bicarbonate in MeOH) (3.0 mg, 1.6 μmol) in a reaction vessel. After drying [^{18}F]TBAF solution at 110 °C for 10 min to remove water and MeOH, three extra portions of CH_3CN were added and dried with N_2 flow at 110 °C for 3 min respectively. A solution of precursor **8** (1.0 mg, 2.0 μmol) in anhydrous DMSO (500 μL) was then added. The vessel was heated at 170 °C for 20 min. Upon completion, the reaction mixture was diluted with water (4.0 mL) and passed through a Waters Sep-Pak Light C18 cartridge. The organic compounds were trapped on the cartridge, 5.0 mL water was used for washing, aimed to remove DMSO residue. After that, the crude product was collected by washing the cartridge with 0.5 mL CH_3CN, diluted with 4.5 mL water and then injected into a radioHPLC system. HPLC purification was performed on a Luna 5 C18(2) 100 Å column (10 mm × 250 mm, 5 μm) using a mobile phase of CH_3CN/ammonium formate (AMF) (0.1 mol/L) (25/75, *v*/*v*) at a flow rate of 5.0 mL/min. The retention time of [^{18}F]AZD9574 is 16.1 min. The radioactive fraction corresponding to the desired product was collected in a sterile flask, diluted with 10.0 mL of water, trapped on a Waters Sep-Pak light C18 cartridge. After washing with 10 mL of water to remove CH_3CN residue, the product was washed out from the cartridge with 0.5 mL of ethanol. The synthetic time was 80 min from the end of bombardment. Radiochemical and chemical purity was measured by an analytical radioHPLC (X-Select™ HSS T3 column, 4.6 mm × 150 mm, 3.5 μm) using a mobile phase of CH_3CN/water with 0.1% TEA (20/80, *v*/*v*) at a flow rate of 1.0 mL/min. The identity of [^{18}F]AZD9574 was confirmed by the co-injection with unlabeled compound AZD9574. Radiochemical yield was 25% non-decay-corrected based on [^{18}F]F^- with >99% radiochemical purity.

4.2. Pharmacology, physicochemical and ADME properties

4.2.1. PARP enzymatic activity assay

PARP enzymatic activity assay was performed in the buffer of 50 mmol/L Tris−HCl (pH 8.0), 50 mmol/L NaCl, 10 mmol/L $MgCl_2$, 0.01% Brij35, 1 mmol/L DTT, 1% DMSO, and 10 μg/mL activated DNA (Sigma, D4522). The PARP1 reaction condition was 2.5 nmol/L PARP1 (RBC, PAR-21-346) and 0.01 mg/mL Core Histones from chicken (RBC, HMT-35-435). The PARP2 reaction condition was 25 nmol/L PARP2 (RBC, PAR-21-347) and 5 μmol/L Histone H3.3 (RBC, HMT-11-134). PARP enzyme and histone substrate were incubated with a series concentration of compounds for 20 min at room temperature, respectively. NAD (Sigma−Aldrich, N1636) was added with a final concentration of 0.5 μmol/L to initiate the reaction and incubate at room temperature for 2 h. Finally, the unreacted NAD was detected by the NAD/NADH-Glo™ kit (Promega, G9071). The IC_{50} values of compounds were obtained by nonlinear regression curve fitting using GraphPad Prism software with "sigmoidal dose−response (variable slope)" four parameters with Hill Slope.

4.2.2. *Partition coefficient (LogP)*

The general procedure for the measurement of partition coefficient (Log*P*) ("shake flask method") was described previously with minor revision in this work[48-49]. Briefly, the measurement of Log*P* value was performed by mixing [^{18}F]AZD9574 (50 μL, 20 μmol/L in DMSO) with *n*-octanol (475 μL) and water (475 μL) in a test tube. The *n*-octanol and water were pre-saturated with each other before use. The tube was vortexed for 1 min before being shaken at 37 °C overnight. Aqueous phase and *n*-octanol phase (200 μL each) were aliquoted. The amount of the test compound in each phase was determined by HPLC equipped with radio-HPLC detector. The Log*P* was calculated by Log (ratio between the amount of [^{18}F] AZD9574 in *n*-octanol and aqueous phase). The procedure was repeated at least triplicate, and the results are shown in Table 1.

4.2.3. *CYP interactions*

The general procedure for CYP interactions was probed according to the reported methods[50-51].

4.3. *Molecular docking*

Computational modelling of PARP1 was based on the 1.85 Å resolution crystal structure bound to an inhibitor (PDB 7ONT)[43]. The model was carefully prepared for docking studies by removing the crystallographic ligand, sulfate ions, and water molecules. Docking studies were performed using AutoDock Vina (v1.2.5), visualization was performed in UCSF ChimeraX (v1.6.1), and two-dimensional protein−ligand interaction plots were made with Schrödinger Maestro (v13.8.135).

4.4. *Stability assay in plasma and liver microsome*

The general procedure for stability measurement was described previously with minor revision in this work[42,52]. All the liver microsome and plasma used in the work was acquired from commercial vendors, including normal mouse plasma serum (Abcam, ab7486), normal rat plasma serum (Abcam, ab7488), normal cynomolgus monkey plasma serum (Abcam, ab155109), and human plasma serum (Sigma−Aldrich, H4522). The radioligand [^{18}F]AZD9574 (20 μL/500 μCi) was added to freshly prepared serum (90 μL) of each species. The mixture was incubated for 30, 60, and 90 min at 37 oc. Aliquots (50 μL) incubated for different time were then transferred to pipes with CH_3CN/H_2O solution (100 μL, 1:1, *v*/*v*) and centrifuged for 10 min (12,000 rpm). The supernatant was harvested and measured by use of analytical HPLC Column (X-Bridge™ Phenyl column, 4.6 mm × 100 mm, 5 μm) with mobile phase of CH_3CN/H_2O (20/80, *v*/*v*) at a flow rate of 1.0 mL/min.

4.5. *In vitro cellular uptake study*

PC-3 cells were purchased from American Type Culture Collection (CRL-1435). PC3 cells were cultured in the F-12k medium with 10% FBS (Corning, 35-010-CF) and 1% penicillin−streptomycin (Life Technologies, 15140122). Cells were maintained at 37 °C in a humidified 5% CO_2 atmosphere. PC3 cells were seeded in 24-well plates at a density of 1×10^5 cells/well 24 h before the uptake assay. The medium was removed, and the cells were rinsed twice with PBS. Then, 1 μCi/well of tracer was added in 0.5 mL of serum-free medium. The cells were incubated at 37 °C for 5, 15, 30, 60, and 120 min. Then, the medium was removed, and cells were rinsed twice with cold PBS and lysed with 0.2 mL 0.1 mol/L NaOH. For the uptake blocking assay, 1.0 μCi/well of tracer with blocking agents was added in 0.5 mL of serum-free medium. The cells were incubated at 37 °C for 60 min. The washing and lysing steps were the same as above. The cell lysis was finally measured by a gamma counter.

4.6. *Autoradiography*

The general procedure for autoradiography was described previously with minor revision in this work[42]. Brain sections (NHP and rat) were pre-incubated with Tris−HCl buffer (50 mmol/L with 0.1% BSA), solution for 10 min at ambient temperature, followed by incubation with [^{18}F]AZD9574 (∼4 μCi/mL, ∼4 nmol/L). For blocking studies, compound AZD9574 (10 μmol/L) and olaparib (Astatech, 12279, 10 μmol/L), known PARP1 inhibitors, were added to incubation solution in advance to determine the specificity of radioligand binding respectively. Similarly, UPF-1035 (MedChemExpress, HY-14477, 10 μmol/L), a known PARP2 inhibitor, was added to incubation solution in advance to determine the specificity of radioligand binding. After incubation for 1 h, brain sections were rinsed with ice-cold buffer with ethanol twice for 2 min, dipped in cold distilled water for 10 s. The brain sections were dried with cold air, then placed on imaging plates (BAS-MS2025, GE Healthcare, NJ, USA) to contact overnight. Autoradiograms were obtained and regions of interest (ROIs) were carefully drawn with reference of naked-eye observation. Radioactivity was measured by an Amersham Typhoon 5 (29187191, GE Healthcare, NJ, USA) and normalized to % of radioactivity *vs*. control. The providers and catalog numbers of other PARP1 inhibitors were listed as follows: AZD2461 (Sigma−Aldrich, SML1858), pamiparib (Cayman Chemical, 33182-5), rucaparib (AstaTech, C74459), veliparib (RayBiotech, 331-10367-4).

4.7. *NHP PET imaging*

Compound [^{18}F]AZD9574 was further evaluated in nonhuman primate PET studies similar to our previously published protocols[52]. Animal information: age 5.5 ± 0.5 years, weight 6.3−7.5 kg, male, rhesus monkeys. The study was performed on a time-of-flight PET/CT scanner (GE Discovery 690, Milwaukee, USA). The monkeys were anesthetized with isoflurane and transferred to a PET scanning bed. CT scans were performed before tracer injection for attenuation correction. After intravenous bolus injection of the tracer (4.05 ± 0.54 mCi), 90 min of three-dimensional dynamic acquisition of brain radioactive signals was performed with 36 frames (6 × 20 s, 8 × 30 s, 4 × 1 min, 5 × 2 min, 5 × 4 min, 4 × 5 min). Magnetic resonance images were acquired from GE 3T scanner (GE DiscoI very 750, Milwaukee, USA). Brain images were acquired using T1-weighted echo sequences in three-dimensional space. Brain reconstruction image processing was performed using PMOD (version 4.105, Bruker preclinical imaging, Fällanden, Switzerland) to perform anatomical position registration. Regions of interest (ROIs) were generated manually under the guidance of MRI structural images and summed PET data. SUV of each VOIs and the corresponding time−activity curves (TACs) were generated for statistical analysis.

4.8. *Western blot protocol for PARP1 expression in PC3 cell lines*

PC-3 cells were purchased from American Type Culture Collection (CRL-1435). PC3 cells were lysed in radioimmunoprecipitation

assay (RIPA) lysis (Thermo Scientific, 89900) and extraction buffer (Thermo Scientific, 89901) with protease and phosphatase Inhibitor Mini Tablets (Thermo Scientific, A32965). The protein concentration was determined using the bicinchoninic acid (BCA) kit (Thermo Scientific, 23227). The following antibodies were used for testing PARP1 and loading control β-tubulin levels: PARP multiclonal antibody (Cell Signaling Technology, 9532), β-tubulin monoclonal antibody (Invitrogen, MA5-16308-D680), and Goat Anti-Rabbit IgG H&L (HRP) secondary antibody (Abcam, ab97080). Images were acquired by ChemiDoc MP Imaging System (Bio-Rad Laboratories, 12003154, San Francisco, USA).

4.9. Western blot protocol for PARP$^{-/-}$ knockout mice and WT brain tissues

The PARP1 KO mouse line 129S-*Parp1*^{tm1Zqw}/J was obtained from Professor Gabriel Corfas' Laboratory (The Jackson Laboratory, 002779). The cerebral cortex was dissected from brains of newborn mice and homogenized using a dounce homogenizer size A in RIPA buffer (Sigma−Aldrich, R0278) with protease and phosphatase inhibitors (Thermo Scientific, 78446) and PARG inhibitor (MedChemExpress, PDD 00017273). The lysates were left on ice for 15 min followed by sonication using a probe sonicator (3 pulses, 2 s each on ice). Then, lysates were vortexed for 30 s followed by centrifugation (M-F24Q, RWD Life Science, TX, USA) at 15,000 rpm for 5 min. Protein concentration in the supernatant was determined using the Pierce BCA Protein Assay Kit (Thermo Scientific, 23227). Then 10 μg of protein in 4 × Laemmli buffer (Bio-Rad, 1610747) and 10% β-mercaptoethanol were subjected to PAGE using 4%−15% Mini-PROTEAN® TGX™ Precast Gel (Bio-Rad, 4561083) at 25 mA per gel for 1 h. Proteins were then transferred to a PVDF membrane with 0.45 μm pore size for 30 min at 10 V using Trans-Blot SD Semi-Dry Transfer Cell (Bio-Rad, 1703940). The PVDF membranes were then incubated in blocking solution (5% bovine serum albumin (Sigma−Aldrich, P02769) in TBST buffer (0.2% Tween20 in TBS)) for 90 min at room temperature, followed by incubation with antibodies against PARP1 (rabbit monoclonal, Cell Signaling, 9532) or α-tubulin (mouse monoclonal, Santa Cruz, sc-23948) at 1:1000 dilution in blocking solution at 4 °C overnight. Thereafter, the blots were washed 5 times for 5 min each in TBST buffer, incubated with the HRP-conjugated secondary antibody in blocking buffer (goat anti-rabbit Cell Signaling at 1:3000, or 1:3000 horse anti-mouse Cell Signaling) for 1 h at room temperature, and then washed again in TBST buffer. The blots were visualized by enhanced chemoluminescence using SuperSignal West Femto Maximum Sensitivity Substrate (Thermo-Scientific, 34095) with a Bio-Rad Chemidoc (Bio-Rad Laboratories, 12003154, San Francisco, USA), and images were analyzed using Bio-Rad Image Lab software (version 3.0.1, Bio-Rad Laboratories, San Francisco, USA).

Acknowledgments

We thank Emory Center for Systems Imaging Radiopharmacy Core (Ron Crowe, Karen B. Dolph, Shane Waldrep) and Department of Radiology and Imaging Sciences, Emory University School of Medicine for general support. Steven H. Liang gratefully acknowledges the support provided, in part, by Emory Radiology Chair Fund and Emory School of Medicine Endowed Directorship (USA). James B. Daunais acknowledges the NIH grant support U01AA014106 and AA028007 (USA). Jimmy S. Patel is the recipient of NCI cancer biology postdoctoral fellowship (T32CA275777, USA).

Author contributions

All authors approved the manuscript through written contributions. Xin Zhou, Jiahui Chen, Jimmy S. Patel, Wenqing Ran, Yinlong Li, Richard S. Van, Mostafa M. H. Ibrahim, Chunyu Zhao, Yabiao Gao, Jian Rong, Ahamd F. Chaudhary, Guocong Li, Junqi Hu, and April T. Davenport performed experiments. James D. Daunais, Yihan Shao, Chongzhao Ran, Thomas L. Collier, Achi Haider, David M. Schuster, Allan I. Levey, Lu Wang and Gabriel Corfas guided the experiments and provided suggestions. Steven H. Liang led the project and contributed to study conceptualization, experiment design and execution. Xin Zhou, Jiahui Chen and Jimmy S. Patel drafted the manuscript and Steven H. Liang performed the final revision. All authors have given approval to the final version of the manuscript. Xin Zhou, Jiahui Chen. and Jimmy S. Patel contributed equally to this work.

Conflicts of interest

The authors have no conflicts of interest to declare.

Appendix A. Supporting information

Supporting information to this article can be found online at https://doi.org/10.1016/j.apsb.2025.05.020.

References

1. Morales J, Li L, Fattah FJ, Dong Y, Bey EA, Patel M, et al. Review of poly (ADP-ribose) polymerase (PARP) mechanisms of action and rationale for targeting in cancer and other diseases. *Crit Rev Eukaryot Gene Expr* 2014;**24**:115−28.
2. Luo X, Kraus WL. On PAR with PARP: cellular stress signaling through poly(ADP-ribose) and PARP-1. *Genes Dev* 2012;**26**:5417−32.
3. Lu Y, Fu W, Xing W, Wu H, Zhang C, Xu D. Transcriptional regulation mechanism of PARP1 and its application in disease treatment. *Epigenetics Chromatin* 2024;**17**:126.
4. Ko HL, Ren EC. Functional Aspects of PARP1 in DNA repair and transcription. *Biomolecules* 2012;**2**:4524−48.
5. Kim G, Ison G, McKee AE, Zhang H, Tang S, Gwise T, et al. FDA approval summary: olaparib monotherapy in patients with deleterious germline BRCA-mutated advanced ovarian cancer treated with three or more lines of chemotherapy. *Clin Cancer Res* 2015;**21**:194257−61.
6. Ledermann JA. PARP inhibitors in ovarian cancer. *Ann Oncol* 2016; **27**(Suppl 1):i40−4.
7. Wolford JE, Bai J, Moore KN, Kristeleit R, Monk BJ, Tewari KS. Cost-effectiveness of niraparib, rucaparib, and olaparib for treatment of platinum-resistant, recurrent ovarian carcinoma. *Gynecol Oncol* 2020;**157**:2500−7.
8. Thapa K, Khan H, Sharma U, Grewal AK, Singh TG. Poly (ADP-ribose) polymerase-1 as a promising drug target for neurodegenerative diseases. *Life Sci* 2021;**267**:118975.
9. Kim C, Chen C, Yu Y. Avoid the trap: targeting PARP1 beyond human malignancy. *Cell Chem Biol* 2021;**28**:4456−62.
10. Curtin NJ, Szabo C. Poly(ADP-ribose) polymerase inhibition: past, present and future. *Nat Rev Drug Discov* 2020;**19**:10711−36.
11. Mao K, Zhang G. The role of PARP1 in neurodegenerative diseases and aging. *FEBS J* 2022;**289**:82013−24.

12. Ryu KW, Kim DS, Kraus WL. New facets in the regulation of gene expression by ADP-ribosylation and poly(ADP-ribose) polymerases. *Chem Rev* 2015;**115**:62453−81.
13. Rong J, Haider A, Jeppesen TE, Josephson L, Liang SH. Radiochemistry for positron emission tomography. *Nat Commun* 2023;**14**: 13257.
14. Willmann JK, van Bruggen N, Dinkelborg LM, Gambhir SS. Molecular imaging in drug development. *Nat Rev Drug Discov* 2008;**7**: 7591−607.
15. Ambur Sankaranarayanan R, Kossatz S, Weber W, Beheshti M, Morgenroth A, Mottaghy FM. Advancements in PARP1 targeted nuclear imaging and theranostic probes. *J Clin Med* 2020;**9**:7.
16. Le Bars D. Fluorine-18 and medical imaging: radiopharmaceuticals for positron emission tomography. *J Fluor Chem* 2006;**127**: 111488−93.
17. Deng X, Rong J, Wang L, Vasdev N, Zhang L, Josephson L, et al. Chemistry for positron emission tomography: recent Advances in ^{11}C-, ^{18}F-, ^{13}N-, and ^{15}O-labeling reactions. *Angew Chem Int Ed Engl* 2019;**58**:92580−605.
18. Matthews PM, Rabiner EA, Passchier J, Gunn RN. Positron emission tomography molecular imaging for drug development. *Br J Clin Pharmacol* 2012;**73**:2175−86.
19. Krishnan HS, Ma L, Vasdev N, Liang SH. (18) F-Labeling of sensitive biomolecules for positron emission tomography. *Chemistry* 2017;**23**: 6215553−77.
20. Puentes LN, Makvandi M, Mach RH. Molecular imaging: PARP-1 and beyond. *J Nucl Med* 2021;**62**:6765−70.
21. Wang Q, Zhang J. Current status and progress in using radiolabelled PARP-1 inhibitors for imaging PARP-1 expression in tumours. *Eur J Med Chem* 2022;**242**:114690.
22. Nguyen NT, Pacelli A, Nader M, Kossatz S. DNA repair enzyme poly(ADP-ribose) polymerase 1/2 (PARP1/2)-targeted nuclear imaging and radiotherapy. *Cancers (Basel)* 2022;**14**:5.
23. Lee HS, Schwarz SW, Schubert EK, Chen DL, Doot RK, Makvandi M, et al. The development of ^{18}F fluorthanatrace: a PET radiotracer for imaging poly (ADP-ribose) polymerase-1. *Radiol Imag Cancer* 2022;**4**:1e210070.
24. Schoder H, Franca PDS, Nakajima R, Burnazi E, Roberts S, Brand C, et al. Safety and feasibility of PARP1/2 imaging with ^{18}F-PARPi in patients with head and neck cancer. *Clin Cancer Res* 2020;**26**:133110−6.
25. Wilson TC, Xavier MA, Knight J, Verhoog S, Torres JB, Mosley M, et al. PET imaging of PARP expression using ^{18}F-Olaparib. *J Nucl Med* 2019;**60**:4504−10.
26. Tong J, Chen B, Tan PW, Kurpiewski S, Cai Z. Poly (ADP-ribose) polymerases as PET imaging targets for central nervous system diseases. *Front Med* 2022;**9**:1062432.
27. Yu J, Luo L, Hu T, Cui Y, Sun X, Gou W, et al. Structure-based design, synthesis, and evaluation of inhibitors with high selectivity for PARP-1 over PARP-2. *Eur J Med Chem* 2022;**227**:113898.
28. Yelamos J, Farres J, Llacuna L, Ampurdanes C, Martin-Caballero J. PARP-1 and PARP-2: new players in tumour development. *Am J Cancer Res* 2011;**1**:3328−46.
29. Coleman RL, Oza AM, Lorusso D, Aghajanian C, Oaknin A, Dean A, et al. Rucaparib maintenance treatment for recurrent ovarian carcinoma after response to platinum therapy (ARIEL3): a randomised, double-blind, placebo-controlled, phase 3 trial. *Lancet* 2017;**390**: 101061949−61.
30. Mirza MR, Monk BJ, Herrstedt J, Oza AM, Mahner S, Redondo A, et al. Niraparib maintenance therapy in platinum-sensitive, recurrent ovarian cancer. *N Engl J Med* 2016;**375**:222154−64.
31. Pujade Lauraine E, Ledermann JA, Selle F, Gebski V, Penson RT, Oza AM, et al. Olaparib tablets as maintenance therapy in patients with platinum-sensitive, relapsed ovarian cancer and a BRCA1/2 mutation ($SOLO_2$/ENGOT-Ov_{21}): a double-blind, randomised, placebo-controlled, phase 3 trial. *Lancet Oncol* 2017;**18**:91274−84.
32. Farres J, Llacuna L, Martin-Caballero J, Martinez C, Lozano JJ, Ampurdanes C, et al. PARP-2 sustains erythropoiesis in mice by limiting replicative stress in erythroid progenitors. *Cell Death Differ* 2015;**22**:71144−57.
33. LaFargue CJ, Dal Molin GZ, Sood AK, Coleman RL. Exploring and comparing adverse events between PARP inhibitors. *Lancet Oncol* 2019;**20**:e15−28.
34. Murnyak B, Kouhsari MC, Hershkovitch R, Kalman B, Marko-Varga G, Klekner A, et al. PARP1 expression and its correlation with survival is tumour molecular subtype dependent in glioblastoma. *Oncotarget* 2017;**8**:2846348−62.
35. Chen B, Ojha DP, Toyonaga T, Tong J, Pracitto R, Thomas MA, et al. Preclinical evaluation of a brain penetrant PARP PET imaging probe in rat glioblastoma and nonhuman primates. *Eur J Nucl Med Mol Imag* 2023;**50**:72081−99.
36. Cortes Gonzalez MA, Jucaite A, Cselenyi Z, Johnstrom P, Pike A, Högnäsbacka A, et al. Discovery, preclinical validation and early human imaging with [^{11}C]AZ14193391 − the first blood-brain barrier permeable and subtype selective PARP1 PET radioligand. *Nucl Med Biol* 2023;**126**−**127**:108465.
37. Johnström P, Johannes J, Pike A, Cselényi Z, Schou M. Abstract 5977: Discovery and preclinical validation of [^{11}C]AZ3391: a first in class blood-brain barrier permeable, subtype selective PARP-1 PET radioligand. *Cancer Res* 2022;**82**:12_Supplement5977.
38. Pike A, Balazs A, Cselényi Z, Degorce SL, Ghosh A, Hande SM, et al. Abstract 5076: evaluation of the CNS penetration of a next generation PARP inhibitor, AZD9574, in cynomolgus monkey using positron emission tomography. *Cancer Res* 2022;**82**: 12_Supplement5076.
39. Staniszewska AD, Pilger D, Gill SJ, Jamal K, Bohin N, Guzzetti S, et al. Preclinical characterization of AZD9574, a blood-brain barrier penetrant inhibitor of PARP1. *Clin Cancer Res* 2024;**30**: 71338−51.
40. Waterhouse RN. Determination of lipophilicity and its use as a predictor of blood-brain barrier penetration of molecular imaging agents. *Mol Imag Biol* 2003;**5**:376−89.
41. Pike VW. Considerations in the development of reversibly binding PET radioligands for brain imaging. *Curr Med Chem* 2016;**23**: 181818−69.
42. Chen Z, Chen J, Chen L, Yoo CH, Rong J, Fu H, et al. Imaging leucine-rich repeat kinase 2 *in vivo* with ^{18}F-labeled positron emission tomography ligand. *J Med Chem* 2023;**66**:31712−24.
43. Johannes JW, Balazs A, Barratt D, Bista M, Chuba MD, Cosulich S, et al. Discovery of 5-{4-[(7-Ethyl-6-oxo-5,6-dihydro-1,5-naphthyridin-3-yl)methyl]piperazin-1-yl}-*N*-methylpyridine-2-carboxamide (AZD5305): a PARP1-DNA trapper with high selectivity for PARP1 over PARP2 and other PARPs. *J Med Chem* 2021;**64**: 1914498−512.
44. Wang ZQ, Auer B, Stingl L, Berghammer H, Haidacher D, Schweiger M, et al. Mice lacking ADPRT and poly(ADP-ribosyl)ation develop normally but are susceptible to skin disease. *Genes Dev* 1995; **9**:5509−20.
45. Zhang X, Zhang Y, Chen Z, Shao T, Van R, Kumata K, et al. Synthesis and preliminary studies of ^{11}C-labeled tetrahydro-1,7-naphthyridine-2-carboxamides for PET imaging of metabotropic glutamate receptor 2. *Theranostics* 2020;**10**:2411178−96.
46. Yu Q, Kumata K, Rong J, Chen Z, Yamasaki T, Chen J, et al. Imaging of transmembrane AMPA receptor regulatory proteins by positron emission tomography. *J Med Chem* 2022;**65**:139144−58.
47. Note_PARP1_Allen_brain_atlas PARP1 expression available at the allen brain atlas database. Available from: https://mouse.brain-map.org/gene/show/11332; 2023.
48. Cheng R, Mori W, Ma L, Alhouayek M, Hatori A, Zhang Y, et al. *In vitro* and *in vivo* evaluation of ^{11}C-labeled azetidinecarboxylates for imaging monoacylglycerol lipase by PET imaging studies. *J Med Chem* 2018;**61**:62278−91.
49. Chen Z, Mori W, Deng X, Cheng R, Ogasawara D, Zhang G, et al. Design, synthesis, and evaluation of reversible and irreversible monoacylglycerol lipase positron emission tomography (PET) tracers

using a "tail switching" strategy on a piperazinyl azetidine skeleton. *J Med Chem* 2019;**62**:73336−53.

50. Deng X, Zhang Y, Chen Z, Kumata K, Van R, Rong J, et al. Synthesis and preliminary evaluation of 4-hydroxy-6-(3-[^{11}C]methoxyphenethyl)pyridazin-3(2*H*)-one, a ^{11}C-labeled D-amino acid oxidase (DAAO) inhibitor for PET imaging. *Bioorg Med Chem Lett* 2020;**30**: 16127326.
51. Sun J, Chen J, Kumata K, Xiao Z, Rong J, Haider A, et al. Imaging the trace amine-associated receptor 1 by positron emission tomography. *Tetrahedron Lett* 2021;**70**:153007.
52. Rong J, Mori W, Xia X, Schafroth MA, Zhao C, Van RS, et al. Novel reversible-binding PET ligands for imaging monoacylglycerol lipase based on the piperazinyl azetidine scaffold. *J Med Chem* 2021;**64**: 1914283−98.